Intrinsic Charm Production in Fixed-Target Experiments at the LHC

R. Vogt

Lawrence Livermore National Laboratory, Livermore, CA 94551, USA
Physics and Astronomy Department, UC Davis, Davis, CA 95616, USA

based on:
RV, arXiv:2101.02858, Phys. Rev. C 103, 035204 (2021)
RV, arXiv:2207.04347, Phys. Rev. C 106, 025201 (2022)
RV, to be submitted

U.S. DEPARTMENT OF ENERGY | Office of Science

Figure 1: This work was performed under the auspices of the U.S. Department of Energy by Lawrence Livermore National Laboratory under Contract DE-AC52-07NA27344, the LLNL-LDRD Program under Projects 21-LW-034 and 23-LW-036 and the HEFTY Collaboration.

Intrinsic Charm is a Long-Standing Puzzle in QCD

Intrinsic charm in the proton $|uudc\bar{c}\rangle$, was first proposed in the 1980's

If this state dominates the wavefunction, the charm quarks carry a larger fraction of the hadron momentum, enhancing charm production in the forward x_F region

A number of experimental hints have been seen, no conclusive results

- **Charm structure function, F_2^c, large at largest x and highest Q^2 measured (EMC)**
- **Leading charm asymmetries consistent with intrinsic charm predictions (D^- over D^+ in $\pi^- p$ interactions, E791)**
- **Double J/ψ production observed at high pair x_F by NA3**
- **Forward charm production observed in many fixed-target experiments (WA82, WA89, E791, SELEX and others)**
- **Proposed explanation of high energy astrophysical neutrino rate at Ice Cube (Brodsky and Laha)**
- **LHCb Z+c-jet measurements at forward rapidity consistent with intrinsic charm**

Global PDF analyses have tried incorporating intrinsic charm and reported a range of possible contributions from 0 to 1%, most lately the NNPDF collaboration (Nature)

Model Calculation

Fixed-target experiments can provide evidence of intrinsic charm

Calculations here are compared to $p+A$ data from the SMOG device with LHCb: $p+\mathrm{Ne}$ at $\sqrt{s_{NN}} = 68.5$ GeV; $p+\mathrm{He}$ at $\sqrt{s_{NN}} = 86.6$ GeV; and $p+\mathrm{Ar}$ at $\sqrt{s_{NN}} = 110.4$ GeV

J/ψ and D^0 measured at backward rapidity in the fixed-target center of mass

The production cross sections are calculated with a combination of perturbative QCD and intrinsic charm contributions; in $p+p$ collisions:

$$\begin{aligned} \sigma_{pp}^{\overline{D}} &= \sigma_{\mathrm{OHF}}(pp) + \sigma_{\mathrm{ic}}^{\overline{D}}(pp) \\ \sigma_{pp}^{J/\psi} &= \sigma_{\mathrm{CEM}}(pp) + \sigma_{\mathrm{ic}}^{J/\psi}(pp) \end{aligned}$$

The D meson and J/ψ cross sections are computed at NLO in the color evaporation model for $p+p$ and $p+A$ interactions; σ_{ic} is the intrinsic charm cross section

In $p+A$ collisions:

$$\begin{aligned} \sigma_{pA}^{\overline{D}} &= \sigma_{\mathrm{OHF}}(pA) + \sigma_{\mathrm{ic}}^{\overline{D}}(pA) \\ \sigma_{pA}^{J/\psi} &= \sigma_{\mathrm{CEM}}(pA) + \sigma_{\mathrm{ic}}^{J/\psi}(pA) \end{aligned}$$

Heavy Flavor Production in Perturbative QCD

The perturbative QCD cross section at NLO for open heavy flavor and quarkonium is

$$\sigma_{\rm OHF}(pp) \;=\; \sum_{i,j}\int_{4m^2}^{\infty} d\hat{s}\int dx_1\,dx_2\;\; F_i^p(x_1,\mu_F^2,k_{T_1})\;\; F_j^p(x_2,\mu_F^2,k_{T_2})\;\; \hat{\sigma}_{ij}(\hat{s},\mu_F^2,\mu_R^2)\;,$$

$$\sigma_{\rm CEM}(pp) \;=\; F_C\sum_{i,j}\int_{4m^2}^{4m_H^2} ds\int dx_1\,dx_2\;\; F_i^p(x_1,\mu_F^2,k_{T_1})\;\; F_j^p(x_2,\mu_F^2,k_{T_2})\;\; \hat{\sigma}_{ij}(\hat{s},\mu_F^2,\mu_R^2)$$

Parton densities factorized into longitudinal (CT10) and a k_T-dependent component to implement k_T broadening a la low p_T resummation; Peterson fragmentation with parameter modified to agree with FONLL included for open charm

$$F^p(x,\mu_F^2,k_T) = f^p(x,\mu_F^2)G_p(k_T)$$

$$G_p(k_T) \;=\; \frac{1}{\pi\langle k_T^2\rangle_p}\exp(-k_T^2/\langle k_T^2\rangle_p)$$

$$\langle k_T^2\rangle_p = \left[1+\frac{1}{n}\ln\left(\frac{\sqrt{s_{NN}}(\mathrm{GeV})}{20\,\mathrm{GeV}}\right)\right]\;\mathrm{GeV}^2$$

$\langle k_T^2\rangle_p$ broadening assumed energy dependent, $n = 12$ from J/ψ data

At $\sqrt{s_{NN}} = 68.5$, 86.6 and 110.4 GeV respectively, $\langle k_T^2\rangle_p = 1.10$, 1.12 and 1.14 GeV^2

D Meson $p+p$ Distributions at SMOG Energies

Uncertainty bands defined by $(m, \mu_F/m_T, \mu_R/m_T) = (1.27 \pm 0.09\,\mathrm{GeV}, 2.1^{+2.55}_{-0.85}, 1.6^{+0.11}_{-0.12})$**;** μ_F**, factorization scale, and** μ_R**, renormalization scale, defined relative to pair transverse mass:** $\mu_{F,R} \propto m_T = \sqrt{m^2 + p_T^2}$ **where** $p_T^2 = 0.5(p_{T_Q}^2 + p_{T_{\overline{Q}}}^2)$

Scale uncertainties set by $\{(\mu_F/m_T, \mu_F/m_T)\} = \{(C,C),\ (H,H),\ (L,L),\ (C,L),\ (L,C),\ (C,H),\ (H,C)\}$ **(Mass uncertainties dominate.)**

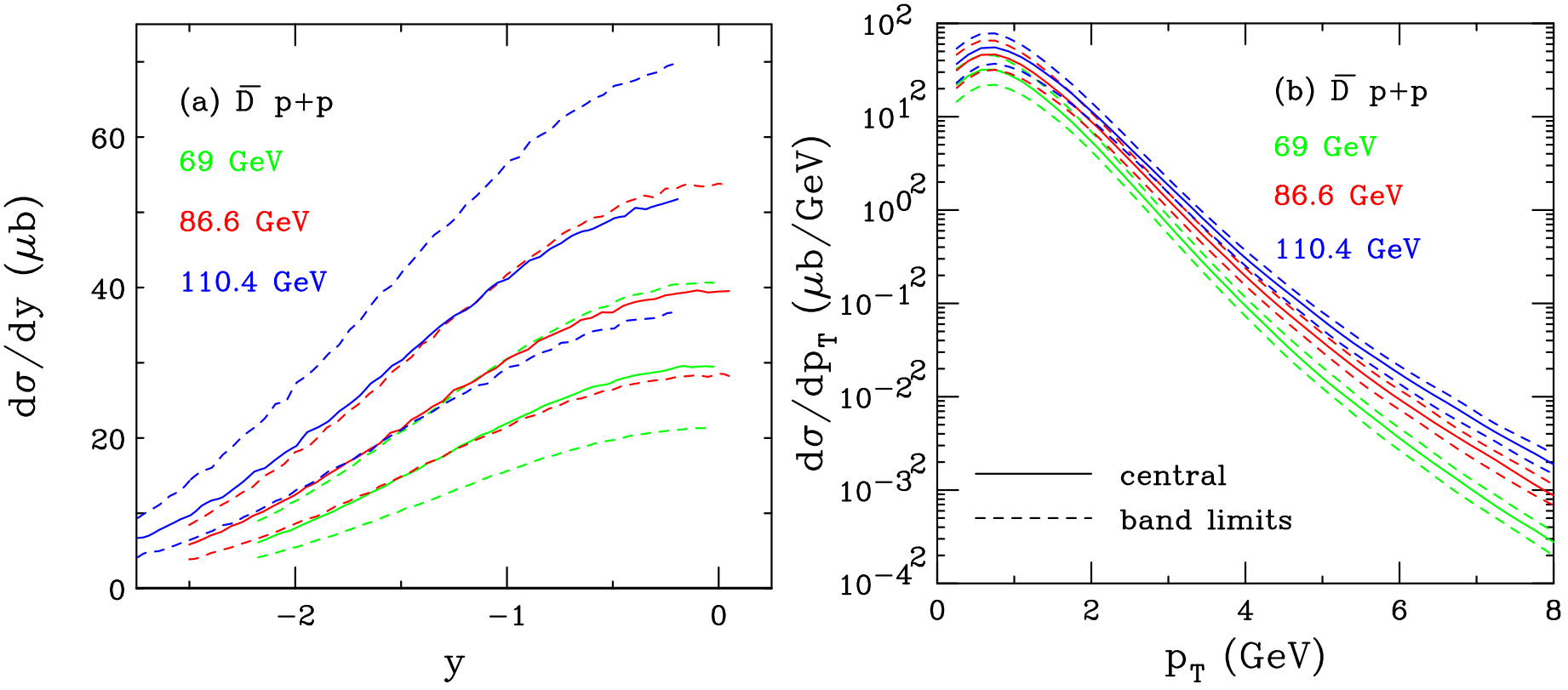

Figure 2: (Color online) The NLO $\overline{D}^0$ production cross sections in $p+p$ collisions at $\sqrt{s}$ = 68.5 (green), 86.6 (red), and 110.4 GeV (blue) as a function of rapidity (a) and p_T (b), in the SMOG fixed-target acceptance, are shown. The solid curves show the central values while the dashed curves outline the upper and lower limits of the uncertainty band.

J/ψ Distributions in $p+p$ at SMOG Energies

CEM normalization F_C set by comparison to total cross section, same value of F_C is used for all uncertainty sets and all energies

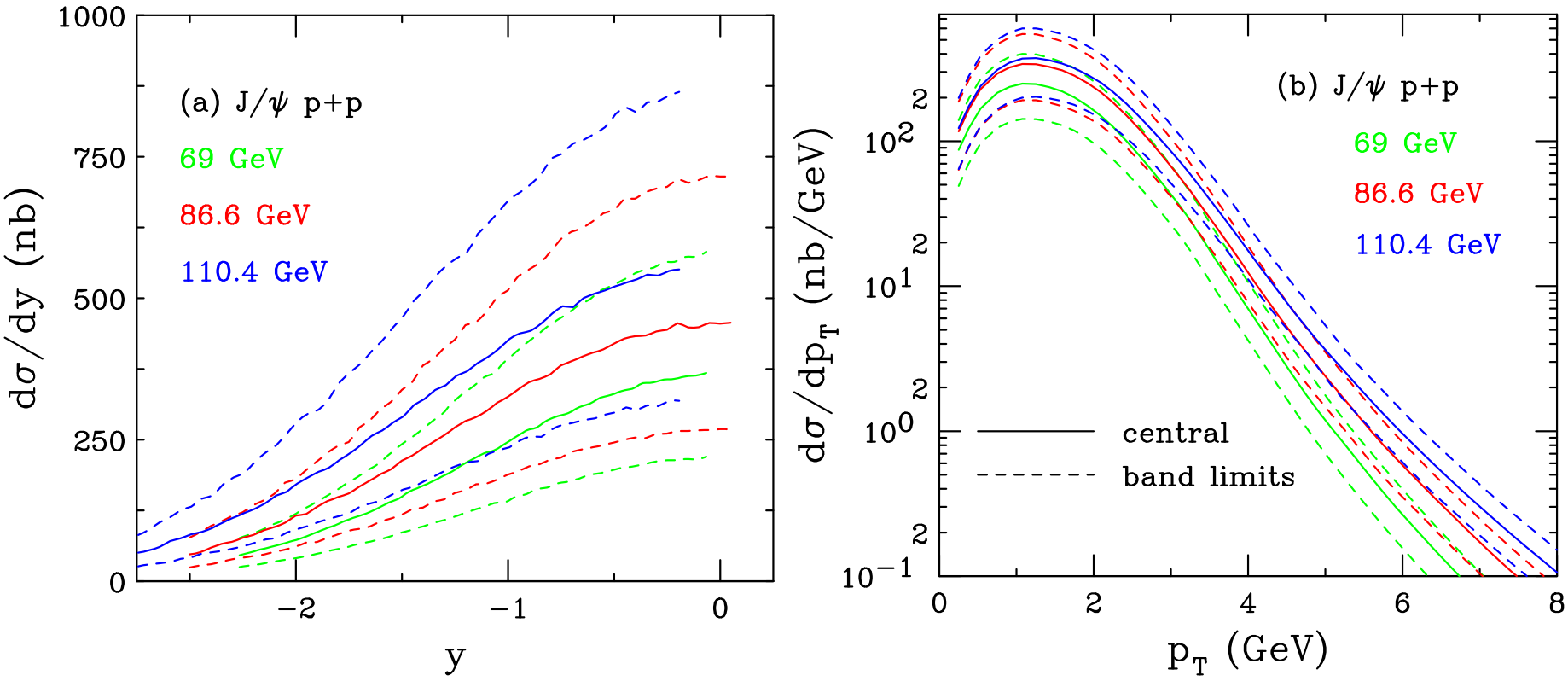

Figure 3: The J/ψ production cross sections in the CEM in $p+p$ collisions at $\sqrt{s} = 68.5$ (green), 86.6 (red), and 110.4 GeV (blue) as a function of rapidity (a) and p_T (b), in the SMOG fixed-target acceptance, is shown. The solid curves show the central values while the dashed curves outline the upper and lower limits of the uncertainty band.

Cold Matter Effects on Perturbative Cross Section

Production cross section in a pA collision is

$$\sigma_{pA} = \sigma_{\rm CEM}(pA) = S_A^{\rm abs} F_C \sum_{i,j} \int_{4m^2}^{4m_H^2} ds \int dx_1\, dx_2\; F_i^p(x_1, \mu_F^2, k_T)\; F_j^A(x_2, \mu_F^2, k_T)\; \hat{\sigma}_{ij}(\hat{s}, \mu_F^2, \mu_R^2)$$

Survival probability for absorption of a (proto)charmonium state in nuclear matter:

$$\begin{aligned}
\sigma_{pA} = \sigma_{pN} S_A^{\rm abs} &= \sigma_{pN} \int d^2b \int_{-\infty}^{\infty} dz\, \rho_A(b,z) S^{\rm abs}(b) \\
&= \sigma_{pN} \int d^2b \int_{-\infty}^{\infty} dz\, \rho_A(b,z) \exp\left\{ - \int_z^{\infty} dz' \rho_A(b,z') \sigma_{\rm abs}(z'-z) \right\}
\end{aligned}$$

The absorption cross section is assumed constant. Prior fixed-target experiments extracted an effective absorption cross section from A^α analysis with $\alpha = 1 - 9\sigma_{\rm abs}/(16\pi r_0^2)$ assuming no other nuclear effects (J/ψ only)

Nuclear parton densities

$$\begin{aligned}
F_j^A(x_2, \mu_F^2, k_T) &= R_j(x_2, \mu_F^2, A) f_j(x_2, \mu_F^2) G_A(k_T) \\
F_i^p(x_1, \mu_F^2, k_T) &= f_i(x_1, \mu_F^2) G_p(k_T)
\end{aligned}$$

$G_A(k_T)$ **includes increased broadening in the nuclear target ($A > 2$)**

k_T Broadening in Nuclei

k_T broadening in nuclei may be enhanced through multiple scattering in the target; to implement enhanced broadening, a larger value of $\langle k_T^2 \rangle$ is used for nuclear targets

$$\langle k_T^2 \rangle_A = \langle k_T^2 \rangle_p + \delta k_T^2$$

δk_T^2 gives strength of broadening

$$\delta k_T^2 = (\langle \nu \rangle - 1)\Delta^2(\mu)$$

The broadening strength depends on the interaction scale:

$$\Delta^2(\mu) = 0.225 \frac{\ln^2(\mu/\mathrm{GeV})}{1 + \ln(\mu/\mathrm{GeV})} \mathrm{GeV}^2 \qquad \mu = 2m_c$$

Strength also depends on number of scatterings proton undergoes passing through nuclear target, $\langle \nu \rangle - 1$

$$\langle \nu \rangle = \sigma_{pp}^{\mathrm{in}} \frac{\int d^2b T_A^2(b)}{\int d^2b T_A(b)} = \frac{3}{2} \rho_0 R_A \sigma_{pp}^{\mathrm{in}}$$

T_A is the nuclear profile function, here $\rho_0 = 0.16/\mathrm{fm}^3$, $R_A = 1.2A^{1/3}$, and the inelastic $p + p$ cross section is $\sigma_{pp}^{\mathrm{in}} \sim 30$ mb for the energies considered here

For helium, neon, and argon targets, $\delta k_T^2 = 0.05$, 0.15, and 0.22 GeV^2 respectively, giving an average broadening of $\langle k_T^2 \rangle_A = 1.17$, 1.25, and 1.36 GeV^2 for $p + \mathrm{He}$, $p + \mathrm{Ne}$ and $p + \mathrm{Ar}$ respectively

Nuclear Modification of the Parton Densities

EPPS16 nuclear parton density modifications differentiate between u and d valence quarks and all sea quarks; 20 parameters give 40 error sets + 1 central set

Uncertainties are determined by calculating cross section for each A with all error sets, adding differences around central set for each parameter in quadrature

Lower energies probe higher x, for $0 < y < 1$, the momentum fraction in the nucleus is in the antishadowing and EMC regions (see right-hand plot)

$$f_j^A(x_2, \mu_F^2) = R_j(x_2, \mu_F^2, A) f_j^p(x_2, \mu_F^2)$$

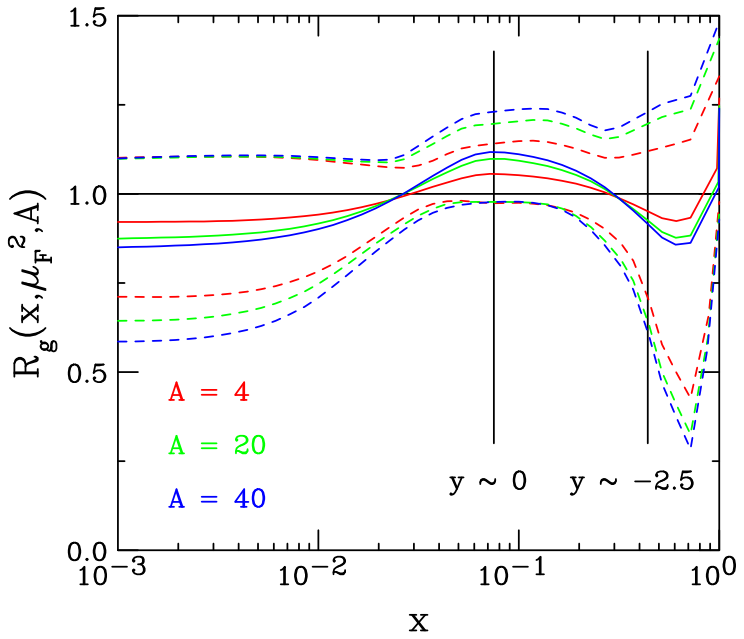

Figure 4: (Color online) The EPPS16 ratios, with uncertainties, are shown at the scale of the J/ψ mass for gluons as a function of momentum fraction x. The central set is denoted by the solid curves while the dashed curves give the upper and lower limits of the uncertainty bands. The results are given for $A = 4$ (red), 20 (green), and 40 (blue). The vertical lines indicate the x range of the SMOG device, $0.075 < x < 0.44$.

Energy Dependence of $\sigma_{\rm abs}^{J/\psi}$

At midrapidity, systematic decrease of $\sigma_{\rm abs}^{J/\psi}$ with $\sqrt{s_{NN}}$, independent of shadowing, trend continues at RHIC and above

$\sigma_{\rm abs}^{J/\psi}(y_{\rm cms}=0)$ at 158 GeV is significantly larger than that measured at 450 GeV

Values of $\sigma_{\rm abs}=4$, 3.5, and 3 mb are used at $\sqrt{s_{NN}}=68.5$, 86.6 and 110.4 GeV

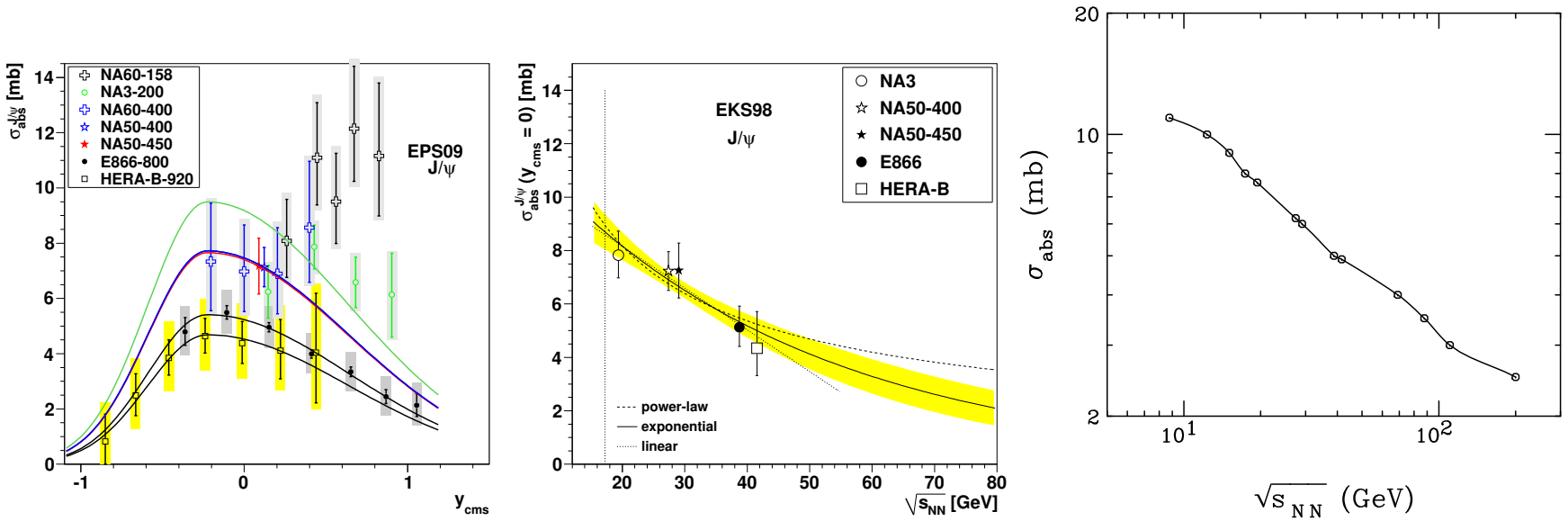

Figure 5: Left: Dependence of $\sigma_{\rm abs}^{J/\psi}$ on $y_{\rm cms}$ for all available data sets including EPS09 shadowing. The shape of the curves is fixed by the E866 and HERA-B data. [Lourenço, RV, Wöhri] Middle: The extracted energy dependence of $\sigma_{\rm abs}^{J/\psi}$ at midrapidity for power law (dashed), exponential (solid) and linear (dotted) approximations to $\sigma_{\rm abs}^{J/\psi}(y=0,\sqrt{s_{NN}})$ using the EKS98 shadowing parameterization with the CTEQ61L parton densities. The band around the exponential curve indicates the uncertainty in the extracted cross sections at $x_F\sim 0$ from NA3, NA50 at 400 and 450 GeV, E866 and HERA-B. The vertical dotted line indicates the energy of the Pb+Pb and In+In collisions at the CERN SPS. [Lourenço, RV, Wöhri] Right: The value of $\sigma_{\rm abs}$ as a function of $\sqrt{s_{NN}}$. The points show the energies used here. The line is meant to guide the eye.

Intrinsic Charm

Probability distribution of five-particle Fock state of the proton:

$$dP_{\mathrm{ic}\,5} = P^0_{\mathrm{ic}\,5} N_5 \int dx_1 \cdots dx_5 \int dk_{x\,1} \cdots dk_{x\,5} \int dk_{y\,1} \cdots dk_{y\,5} \frac{\delta(1-\sum_{i=1}^5 x_i)\delta(\sum_{i=1}^5 k_{x\,i})\delta(\sum_{i=1}^5 k_{y\,i})}{(m_p^2 - \sum_{i=1}^5 (\widehat{m}_i^2/x_i))^2}$$

$i = 1, 2, 3$ are u, u, d light quarks, 4 and 5 are c and $\overline{c}$, N_t normalizes the probability to unity and P^0_{ic} scales the normalized probability to the assumed intrinsic charm content: 0.1%, 0.31% and 1% are used to represent the range of probabilities assumed previously

The IC cross section is determined from soft interaction scale breaking coherence of the Fock state, $\mu^2 = 0.1$ GeV^2

$$\sigma_{\mathrm{ic}}(pp) = P_{\mathrm{ic}\,5} \sigma^{\mathrm{in}}_{pN} \frac{\mu^2}{4\widehat{m}_c^2}$$

The cross sections from intrinsic charm are then obtained by multiplying by the normalization factor for the CEM to the J/ψ while we assume direct correspondence with IC cross section for $\overline{D}^0$

$$\sigma^{\overline{D}}_{\mathrm{ic}}(pp) = F_C \sigma_{\mathrm{ic}}(pp) \quad , \sigma^{J/\psi}_{\mathrm{ic}}(pp) = F_C \sigma_{\mathrm{ic}}(pp)$$

The A dependence is the same for both $\overline{D}$ and J/ψ

$$\sigma_{\mathrm{ic}}(pA) = \sigma_{\mathrm{ic}}(pp)\, A^\beta$$

where $\beta = 0.71$ for a proton beam on a nuclear target, as determined by NA3

LHCb: Evidence of Intrinsic Charm in $Z + c$-Jet Events

$Z+c$-jet ratio to Z+all-jet events at $\sqrt{s} = 13$ TeV is more consistent with calculations including intrinsic charm at high $y(Z)$, up to 1% intrinsic charm content

Differences between calculations without intrinsic charm (no IC) and intrinsic charm allowed calculations, either with NNPDF 3.0 including IC or CT14 with a 1% IC content, grows larger with increasing $y(Z)$

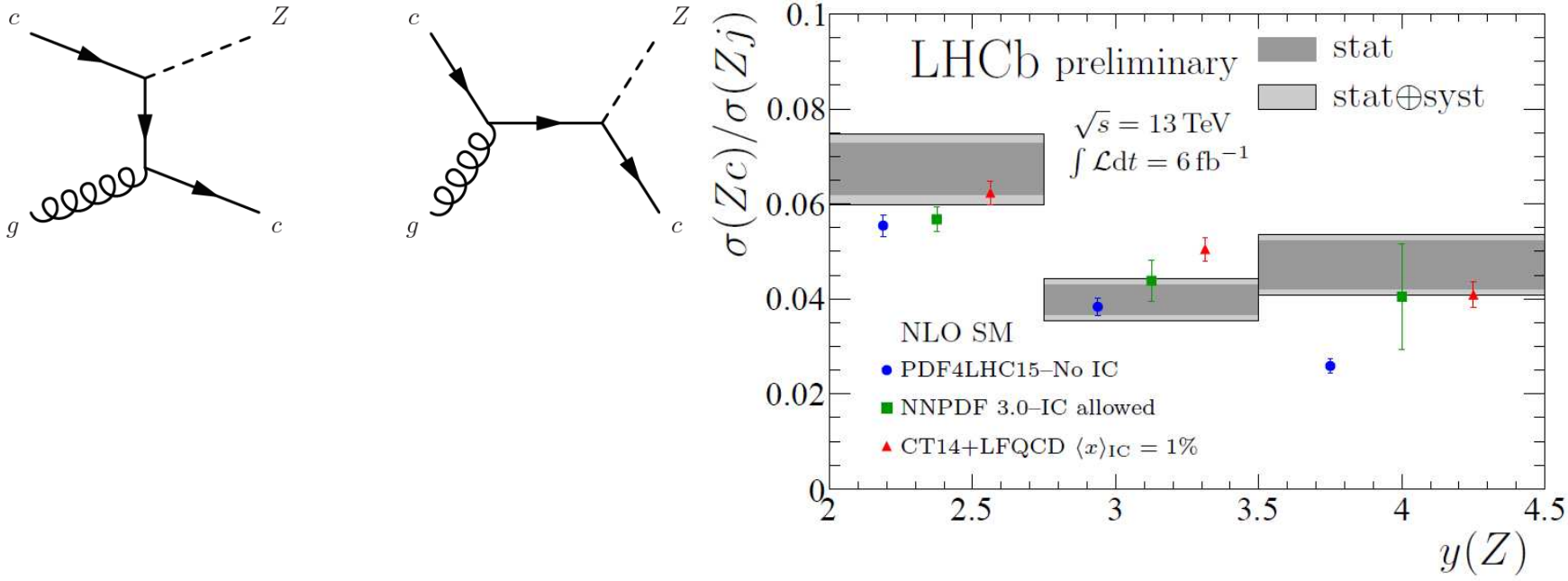

Figure 6: (Left) Leading order diagrams producing $Z + c$-jet events. (Right) Ratio of $Z + c$-jets to Z+all-jet events from LHCb. LHCb data from PRL **128**, 082001 (2022).

Intrinsic Charm Boosted at Forward Rapidity

As $\sqrt{s_{NN}}$ increases, the intrinsic charm rapidity distribution is moved further away from midrapidity, at collider energies it is inaccessible to most forward detectors

The p_T distributions are shown with the rapidity range is restricted to $0 < y < 1$, green curve shows integration over all y; if y acceptance at higher y, more of the IC p_T distribution is captured

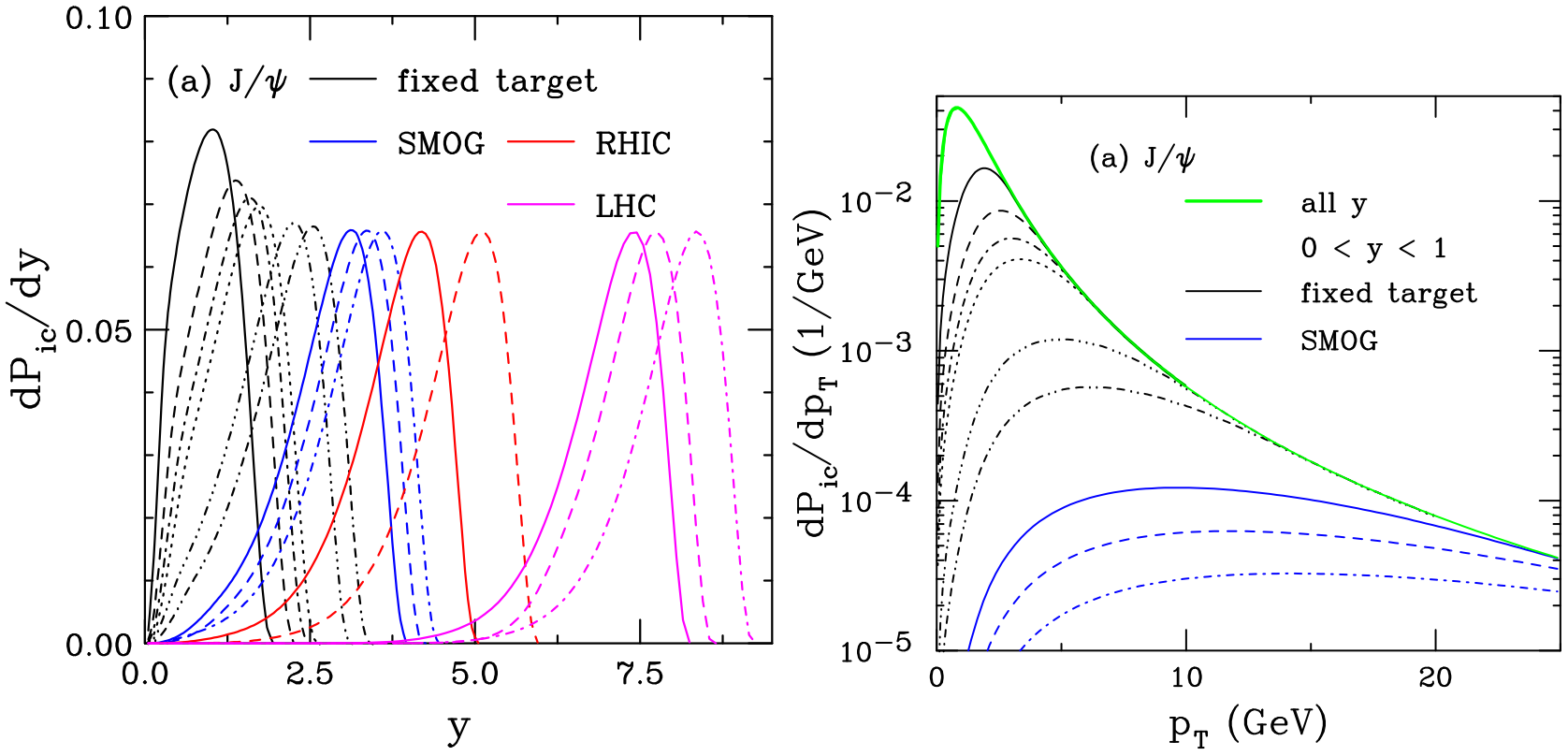

Figure 7: The probability distributions for J/ψ production from a five-particle proton Fock state as a function of y (left) and p_T (right). The rapidity distributions are shown for $\sqrt{s} = 8.8$ GeV to 13 TeV. (Right) The results are shown for all rapidity in the solid green curve. Results for restricting the rapidity range to $0 < y < 1$ are shown for $p_{\rm lab} = 40$, 80 and 120 GeV by the solid black, dashed blue and dot-dashed red respectively.

Summary of Previous Fixed-Target J/ψ Data

NA60 $p_{\rm lab} = 158$ **and 400 GeV, covering** $0.05 < x_F < 0.4$ **and** $-0.075 < x_F < 0.125$ **respectively, were taken on Be, Al, Cu, In, W, Pb, and U targets (PLB 706, 263 (2012))**

NA3 $p_{\rm lab} = 200$ **GeV,** $x_F > 0$**, taken on a Pt target (Z. Phys. C 20, 101 (1983))**

NA50 $p_{\rm lab} = 450$ **GeV, midrapidity** $(-0.1 < x_F < 0.1)$**, used Be, Al, Cu, Ag, W and Pb targets (EPJ C 33, 31 (2004))**

E866 $p_{\rm lab} = 800$ **GeV,** $-0.09 < x_F < 0.95$**, used Be, Fe, and W targets (PRL 84, 3256 (2000))**

HERA-B $p_{\rm lab} = 920$ **GeV,** $-0.34 < x_F < 0.14$**, used C, Ti and W targets (EPJ C 60, 525 (2009))**

E866 J/ψ x_F and p_T Distributions $(p+p)$

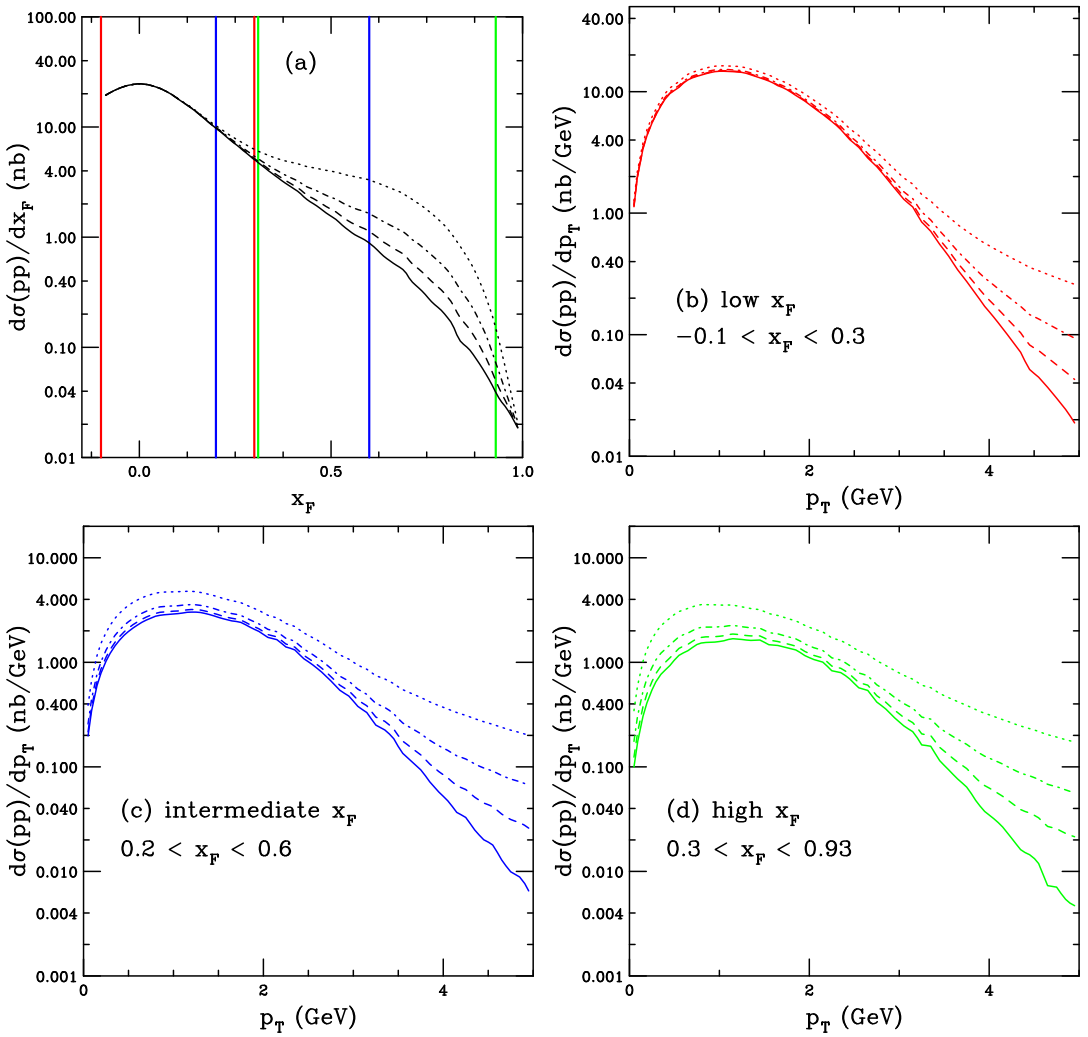

Figure 8: The J/ψ cross sections in $p+p$ collisions at $\sqrt{s} = 38.8$ GeV with and without IC as a function of x_F (a) and p_T at low (b), intermediate (c), and high x_F (d). The solid curves do not include IC while the dashed, dot-dashed and dotted curves use $P^0_{\mathrm{ic}\,5} = 0.1\%$, 0.31% and 1% respectively. The colored vertical bars on the x_F distributions show the x_F limits of the p_T distributions in (b)-(d) and matches the color of the curves in (b)-(d). RV, PRC **103**, 035204 (2021).

Comparison with α Extracted from E866 J/ψ $p+A$ Data

E866 obained α as a function of x_F and p_T (in 3 x_F bins) for $A =$ Be, Fe, and W

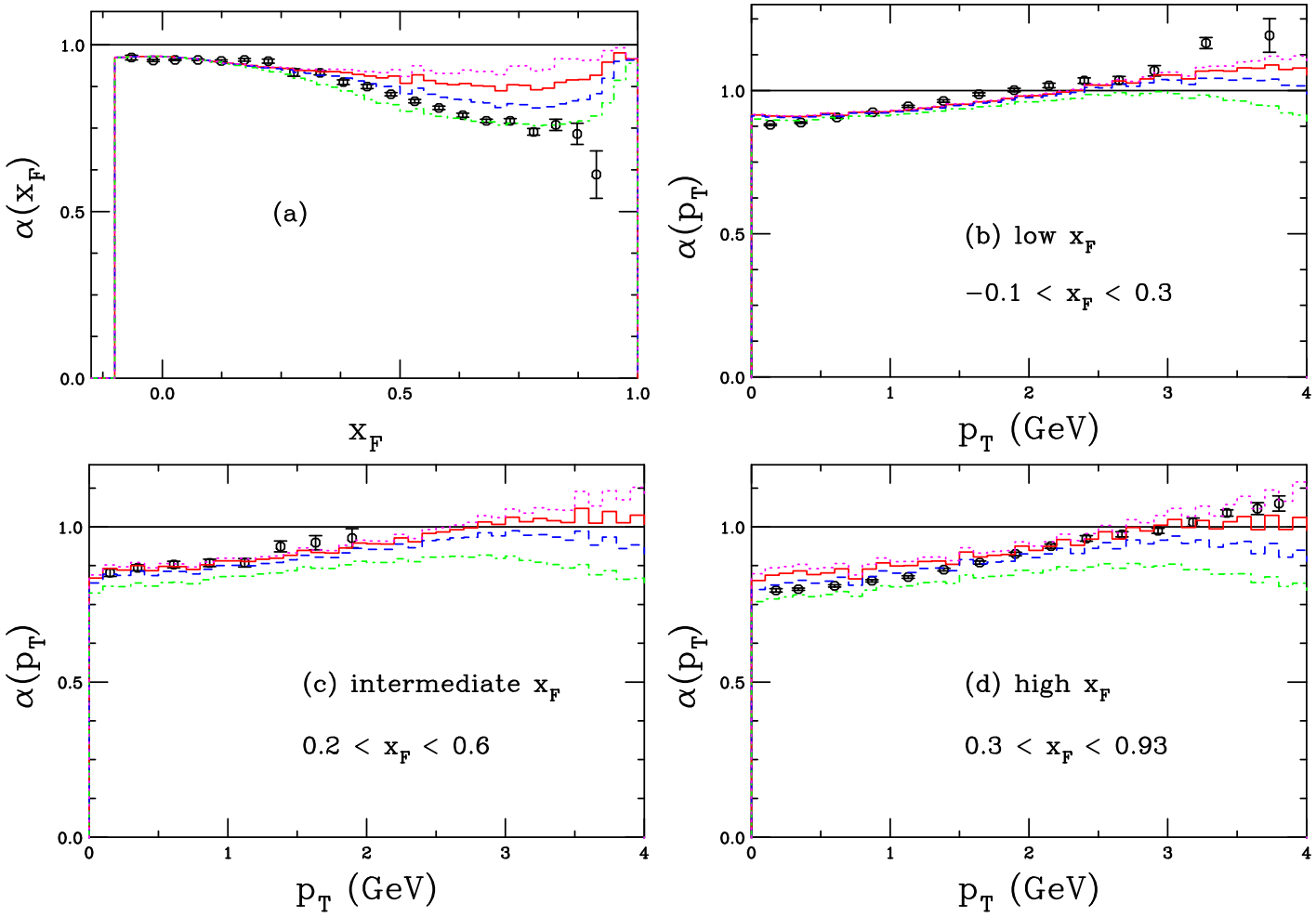

Figure 9: The exponent $\alpha(x_F)$ (a) and $\alpha(p_T)$ for low x_F (b), intermediate x_F (c), and high x_F (d). The dotted magenda curves use $P^0_{\mathrm{ic}\,5} = 0$ while the solid red, dashed blue, and dot-dashed green curves show $P^0_{\mathrm{ic}\,5} = 0.1\%$, 0.31% and 1% respectively. The E866 data (PRL **84**, 3256 (2000)) are the black points. From: RV, PRC **103**, 035204 (2021).

Comparison of $\alpha(x_F)$ with Fixed-Target J/ψ Data

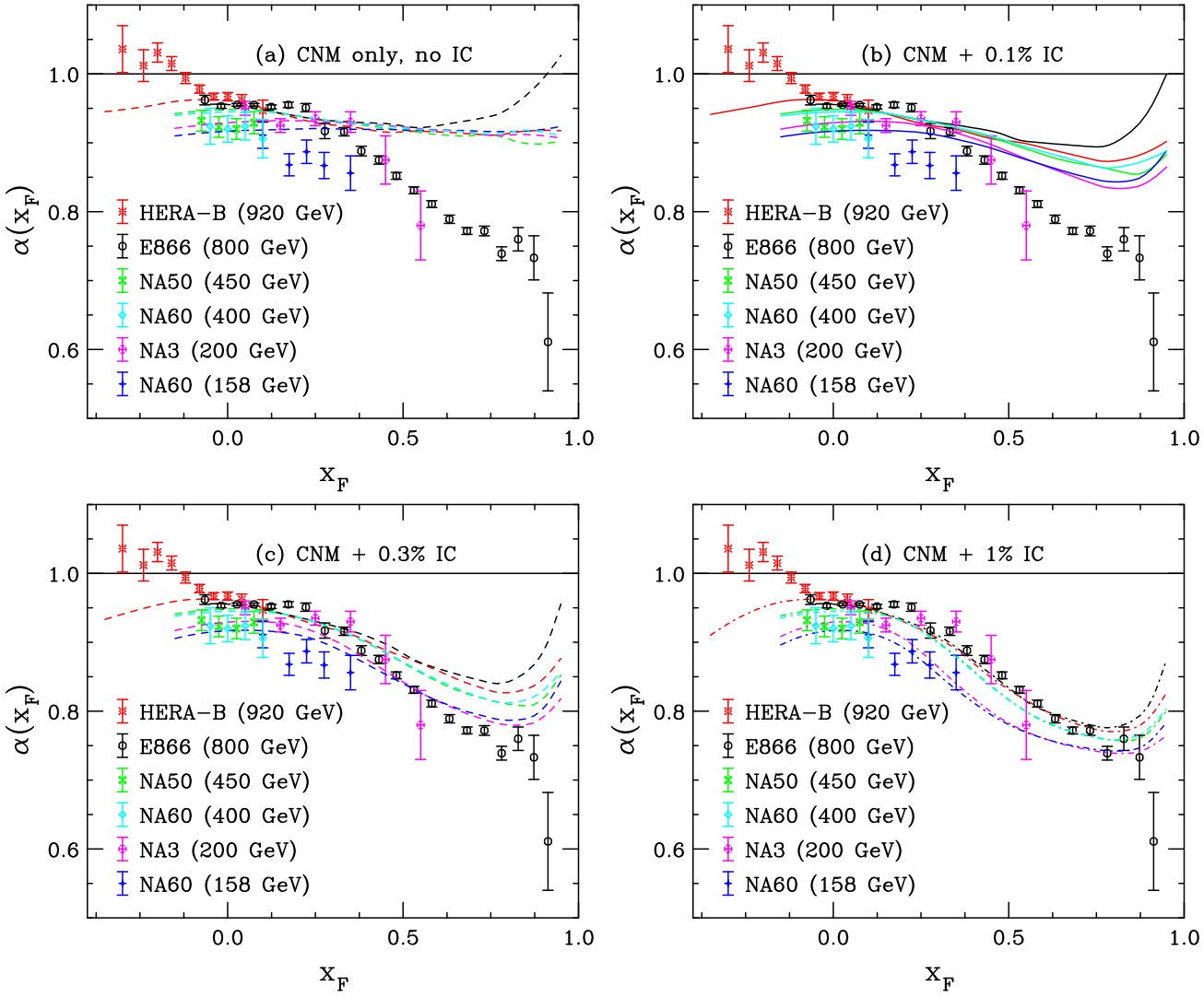

Figure 10: The value of $\alpha(x_F)$ for J/ψ production at: NA60 ($p_{\rm lab} = 158$ GeV), NA3 ($p_{\rm lab} = 200$ GeV), NA60 ($p_{\rm lab} = 400$ GeV), NA50 ($p_{\rm lab} = 450$ GeV), E866 ($p_{\rm lab} = 800$ GeV), and HERA-B ($p_{\rm lab} = 920$ GeV). The points and curves of the same color are at the same energy. Calculations with $P^0_{\rm ic\,5} = 0$ are in (a) while $P^0_{\rm ic\,5} = 0.1\%$, 0.3%, and 1% are shown in (b)-(d).

SMOG $\overline{D}^0$ Results Compared to Calculations

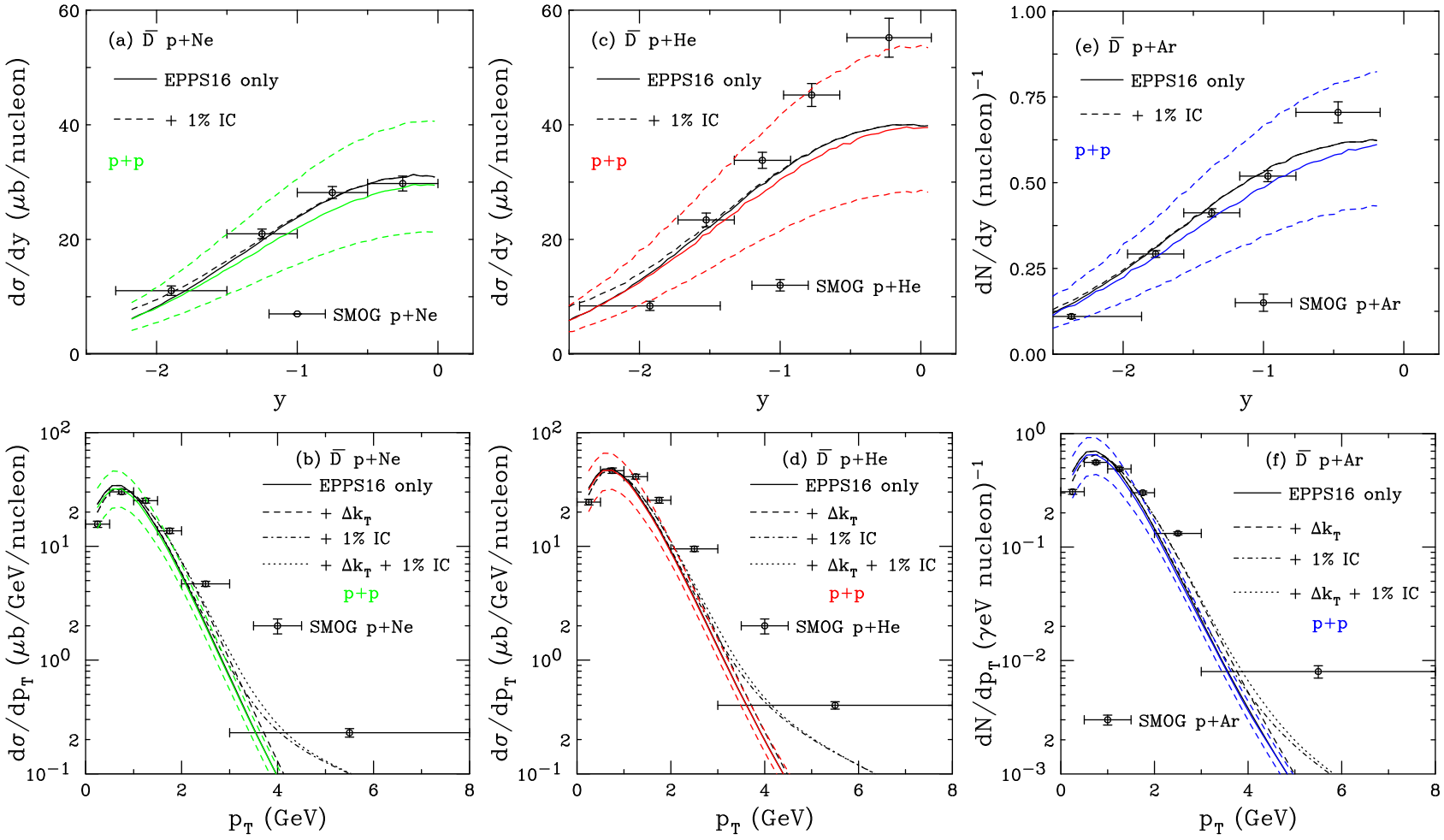

Figure 11: The $\overline{D}$ cross section as a function of y in (a), (c), (e) and p_T in (b), (d), (f) for $p+$Ne ($\sqrt{s_{NN}} = 68.5$ GeV) in (a) and (b); $p+$He ($\sqrt{s_{NN}} = 86.6$ GeV) in (c) and (d); and $p+$Ar ($\sqrt{s_{NN}} = 110.4$ GeV) in (e) and (f). The black curves are the $p+A$ calculations. The colored curves (solid and dashed) show the QCD $p+p$ calculations (no IC). The $p+A$ rapidity distributions are shown for EPPS16 only (solid) and EPPS16 with $P^0_{\rm ic\,5} = 1\%$ (dashed). The p_T distributions show EPPS16 only (solid); EPPS16 with k_T kick (dashed); EPPS16 and $P^0_{\rm ic\,5} = 1\%$ (dot-dashed); and EPPS16, k_T kick and $P^0_{\rm ic\,5} = 1\%$ (dotted). The $p+$Ne data are from arXiv:2211.11633; the $p+$He and $p+$Ar data are from PRL **122**, 132002 (2019).

SMOG J/ψ Results Compared to Calculations

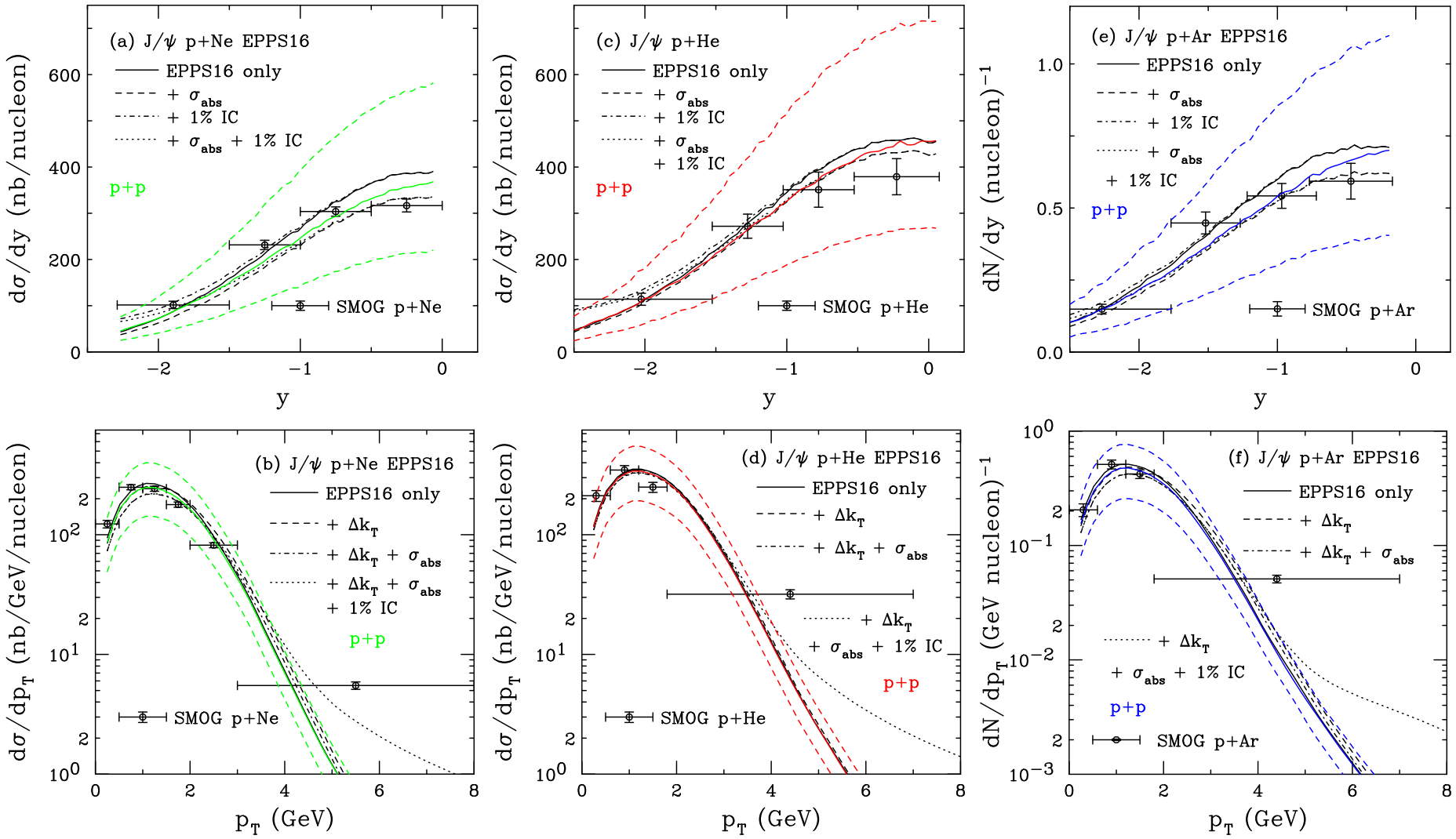

Figure 12: The J/ψ cross section as a function of y in (a), (c), (e) and p_T in (b), (d), (f) for p+Ne ($\sqrt{s_{NN}} = 68.5$ GeV) in (a) and (b); p+He ($\sqrt{s_{NN}} = 86.6$ GeV) in (c) and (d); and $p + $ Ar ($\sqrt{s_{NN}} = 110.4$ GeV) in (e) and (f). The black curves are the $p + A$ calculations. The colored curves (solid and dashed) show the CEM $p + p$ calculations (no IC). The $p + A$ rapidity distributions are shown for EPPS16 only (solid); EPPS16 with absorption (dashed); EPPS16 and $P^0_{\rm ic\,5} = 1\%$ (dot-dashed); and EPPS16, absorption, and $P^0_{\rm ic\,5} = 1\%$ (dotted). The p_T distributions show EPPS16 only (solid); EPPS16 with k_T kick (dashed); EPPS16, absorption, and k_T kick (dot-dashed); and EPPS16, absorption, k_T kick and $P^0_{\rm ic\,5} = 1\%$ (dotted). The $p + $ Ne data are from arXiv:2211.11645; the $p + $ He and $p + $ Ar data are from PRL **122**, 132002 (2019).

Asymmetries Between $\overline{D}^0$ and D^0 Mesons: Leading vs. Non-leading Charm

Assuming 1% IC for leading $\overline{D}^0(\bar{c}u)$ and no IC for non-leading $D^9(c\bar{u})$ underestimates the measured $p+\mathrm{Ne}$ asymmetry (SMOG defined asymmetry as $c-\bar{c}$, not as leading vs. non-leading)

No obvious reason why IC would give finite asymmetry at $y \sim 0$

Maciula and Szczurek included production by recombination with IC which gives larger asymmetry at finite y but no asymmetry at large p_T

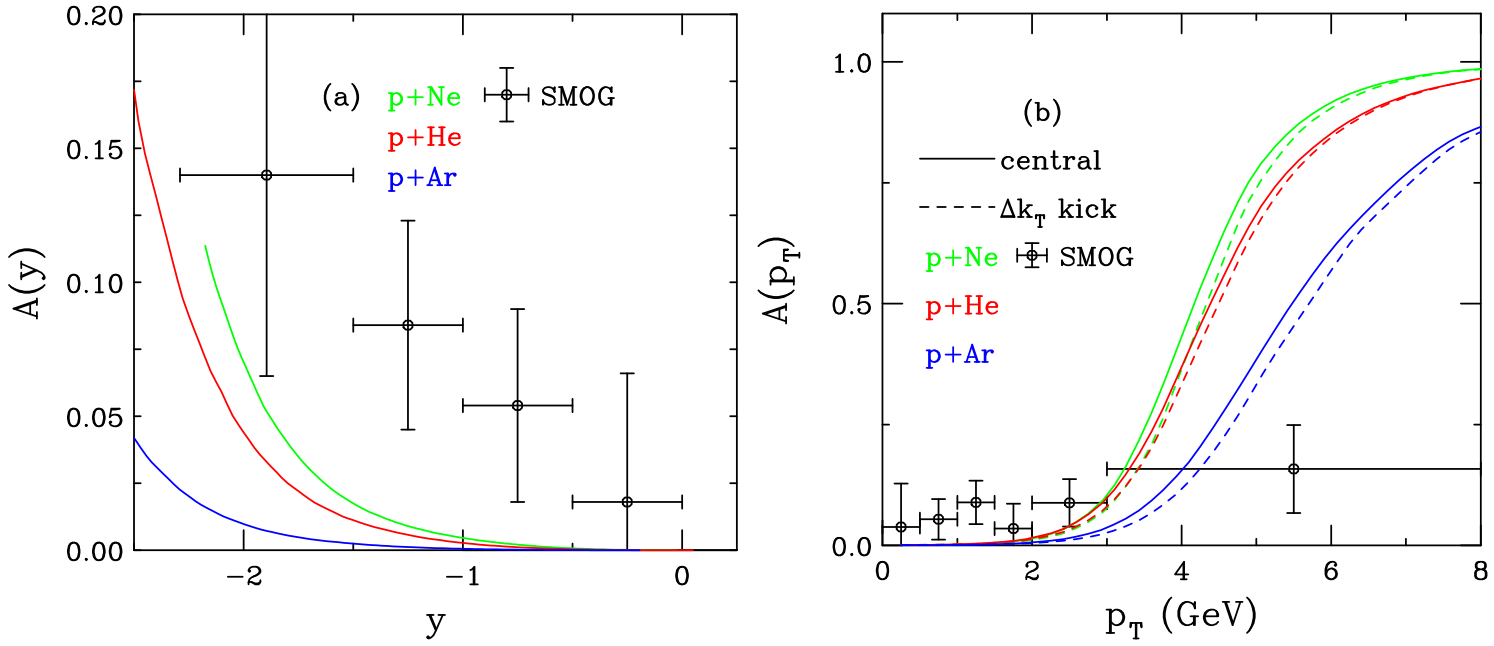

Figure 13: The $\overline{D}$-D asymmetry as a function of rapidity (a) and transverse momentum (b) for $p+\mathrm{Ne}$ collisions at $\sqrt{s_{NN}} = 68.5$ GeV (green); $p+\mathrm{He}$ collisions at $\sqrt{s_{NN}} = 86.6$ GeV (red); and $p+\mathrm{Ar}$ collisions at $\sqrt{s_{NN}} = 110.4$ GeV (blue). All calculations include the EPPS16 central set and $P^0_{\mathrm{ic}\,5} = 1\%$. In (b) the dashed curves also include a k_T kick. Data from arXiv:2211.11633.

Summary

Model calculations in good agreement with the SMOG $p+A$ cross section data but more precise data needed at backward rapidity and high p_T

SMOG data for D^0 production asymmetry stronger at $y \sim 0$ than calculated with 1% IC (considered maximum contribution)

Other fixed-target data, as from NA60+, would be useful to study potentially larger IC contributions closer to midrapidity

IC may also be useful for studying exotic hadron structure: studies with $|uudb\bar{b}b\bar{b}\rangle$ states showed that the proposed double Υ state reported (average mass 18.15 GeV) by the A_NDY Collaboration was smaller than calculated mass of the state but compatible with proposed $b\bar{b}b\bar{b}$ tetraquark masses (PRD 104, 094025 (2021))

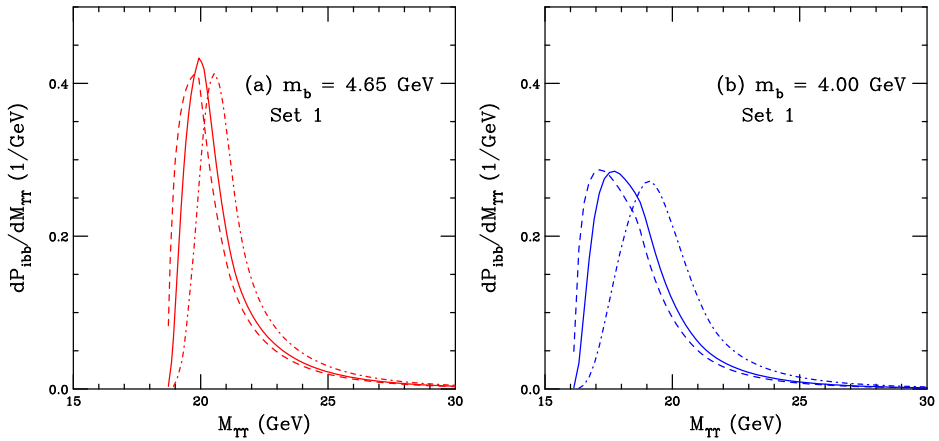

Figure 14: The probability for double Υ production from a seven-particle Fock state as a function of the pair mass for three different k_T integration ranges are shown: $k_q^{\max} = 0.2$ GeV, $k_b^{\max} = 1.0$ GeV and $k_\Upsilon^{\max} = 1.0$ GeV (solid); $k_q^{\max} = 0.1$ GeV, $k_b^{\max} = 0.5$ GeV and $k_\Upsilon^{\max} = 0.5$ GeV (dashed); and $k_q^{\max} = 0.4$ GeV, $k_b^{\max} = 2.0$ GeV and $k_\Upsilon^{\max} = 2.0$ GeV (dot-dashed). All distributions are normalized to unity. In (a) $m_b = 4.65$ GeV while in (b) $m_b = 4.0$ GeV. From PRD **104**, 094025 (2021).